Solar Energy 205 (2020) 349–357

Contents lists available at ScienceDirect

Solar Energy

journal homepage: www.elsevier.com/locate/solener

Experimental and SCAPS simulated formamidinium perovskite solar cells: A comparison of device performance

S. Karthick[a,c], S. Velumani[a,b,*], J. Bouclé[c,*]

[a] Program on Nanoscience and Nanotechnology, Centro de Investigación y de Estudios Avanzados del Instituto Politécnico Nacional (CINVESTAV-IPN), Av. Instituto Politécnico Nacional 2508, Col. San Pedro Zacatenco, Ciudad de México, Código Postal 07360, Mexico

[b] Department of Electrical Engineering (SEES), Centro de Investigación y de Estudios Avanzados del Instituto Politécnico Nacional (CINVESTAV-IPN), Av. Instituto Politécnico Nacional 2508, Col. San Pedro Zacatenco, Ciudad de México, Código Postal 07360, Mexico

[c] Univ. Limoges, CNRS, XLIM, UMR 7252, F-87000 Limoges, France

ARTICLE INFO

Keywords:
Perovskite solar cells
SCAPS-1D simulation
Series and shunt resistances

ABSTRACT

In this study, experimental photovoltaic performance and their numerical SCAPS-1D simulations are compared for methylammonium-free perovskite solar devices based on the formamidinium organic cation. Experimentally, it is established that the incorporation of small amounts of cesium (Cs^+) and bromide (Br^-) into $HC(NH_2)_2PbI_3(FAPI)$ stabilizes the optically active $\alpha - FAPbI_3$ black phase, and boost the power conversion efficiency (PCE) of associated devices from 4 to 15% under standard illumination. The effect of series and shunt resistances (R_{series} & R_{shunt}) were theoretically evaluated and discussed by modeling the electrical characteristics of the cell as a function of active layer composition, using the SCAPS-1D software. Ideal devices built without these parasitic resistances do not match the experimental trends, although they reflect the influence of bandgap edge on the photocurrent generation. Feeding the experimental R_{series} and R_{shunt} values to SCAPS allows us to interpret the main limitations to the device current-voltage characteristics. The instability of the pure *FAPI* phase is responsible for the drastic deterioration in R_{series} and R_{shunt}, ultimately influencing the fill factor. Our data clearly confirm the beneficial effect of mixed cation and mixed halides on device operation.

1. Introduction

One of the greatest strengths and advantage of hybrid perovskites solar cells is their skyrocketing certified power conversion efficiencies over 25% (NREL, 2019), which is due to their excellent properties like tunable band gap, large absorption coefficient, low exciton binding energy, high charge carrier mobility and long diffusion lengths (Eperon et al., 2014; Galkowski et al., 2016; Pang et al., 2014; Shallcross et al., 2017; Zhumekenov et al., 2016). Recently, formamidinum lead iodide perovskite ($FAPbI_3 - 1.48eV$) received tremendous attention compared to methylammonium lead iodide ($MAPbI_3 - 1.55eV$) because of its optimum bandgap value closer to the infra-red single junction range (Eperon et al., 2014). Despite these advantages, the black colored cubic $\alpha - FAPbI_3$ is found to be metastable at room temperature (Han et al., 2016; Wozny et al., 2015). The mixed organic/inorganic cation and/or mixed anion strategies have been shown to be of great help to stabilize the $\alpha - FAPbI_3$, simultaneously suppressing the yellow $\delta - FAPbI_3$ phase which is not suitable for photovoltaic applications. In particular, the incorporation of commonly known organic methylammonium (MA^+)/inorganic Cesium (Cs^+) into the A site or substitution of bromide (Br^-)/chloride (Cl^-) into the X site are now well established to achieve more stable and efficient photocurrent generation. Number of reports are available in the perovskite research community, to explain Cs^+ and Br^- incorporation evidently suppressing the non-perovskite yellow phase of $FAPbI_3$ to steadying the black colored $\alpha - FAPbI_3$ phase (Bush et al., 2017; Groeneveld et al., 2020; Hu et al., 2018; McMeekin et al., 2016; Prathapani et al., 2018; Wang et al., 2017; Yang et al., 2018).

A small amount of Cs^+ incorporated into the pristine $FAPbI_3$ structure ($FA_{1-x}Cs_xPbI_3$) provides superior phase durability over 100 h of light irradiation than unsubstituted $FAPbI_3$. It also exhibits an outstanding resistance against humidity (90% of moisture level for 4 h) compared to the pure phase (Li et al., 2016). This combination of cations quenches the spontaneous phase change from black to yellow or $\delta - phase$, especially due to the preferential formation of CsI which reduces the release of detrimental HI species (Huang et al., 2017; Lee et al., 2015). Finally, the formamidinium-Cesium ($FA - Cs$) combination demonstrates an excellent photostability, thermal stability, and resistance to moisture than the formamidinium-methylammonium

* Corresponding authors.
E-mail addresses: velu@cinvestav.mx (S. Velumani), johann.boucle@unilim.fr (J. Bouclé).

https://doi.org/10.1016/j.solener.2020.05.041
Received 28 March 2020; Received in revised form 11 May 2020; Accepted 16 May 2020

($FA - MA$) pair (Huang et al., 2017; Lee et al., 2015; Prochowicz et al., 2019; Yi et al., 2016; Yu et al., 2016). Regarding the halide site, adding a small amount of Br^- is a well-known strategy towards higher bandgap perovskites (1.5–1.7 eV). The bromide incorporation directly modifies the structural, morphological, hence electrical and optical properties of the material. Especially, a larger strain occurs while halide demixing, which is providing the partial support in order to encounter the halide segregation (Nazarenko et al., 2017; Rehman et al., 2017; Saliba et al., 2016; Sutter-Fella et al., 2018).

In this work, three different types of FA-based perovskite active layers are processed using a one-step solution method and the anti-solvent treatment: (i) pristine $FAPbI_3$, (ii) $FA_{0.85}Cs_{0.15}PbI_3$, and (iii) $FA_{0.85}Cs_{0.15}Pb(I_{0.85}Br_{0.15})_3$. These active layers are integrated to perovskite solar cells using a conventional planar device architecture given by Glass/FTO/SnO_2/Perovskite/Spiro-OMeTAD/Au. In order to get more insight on the influence of Cs^+ and Br^- cation/halogen addition on device performance, experimental current density-voltage characteristics under solar irradiation, as well as scanning electron microscopy (SEM) images and optical spectroscopy spectra are presented. More specifically, simulations of device's electrical responses are made using the Solar Cell Capacitance Simulator (SCAPS-1D) software which allow us to discuss the influence of perovskite composition and its effect on parasitic resistances. Although several simulations using SCAPS have been reported in the literature for perovskite solar cells (Abdelaziz et al., 2020; Azri et al., 2019; Haidari, 2019; Kuang et al., 2018), we especially focus first on ideal devices, which do not account for series or shunt resistance. We then show that the electrical losses are crucial in order to reproduce the trend of experimental devices based on pure FA cation, or on mixed systems ($FA - Cs$ *and* $I - Br$). The impact of phase evolution of the FA-based perovskites under ambient conditions can be nicely reproduced by the simulation in these conditions. This contribution provides novel explanations which is intending to tackle the degradation of $\alpha - FAPbI_3$ perovskite phase as well as to enhance the device PCE. As for as our literature review extends, this is the first report elucidating the correlation between experimental and SCAPS-1D simulated formamidinium organic cation based perovskites solar devices, especially, on pristine $FAPbI_3$, $FA_{0.85}Cs_{0.15}PbI_3$, and $FA_{0.85}Cs_{0.15}Pb(I_{0.85}Br_{0.15})_3$.

2. Experimental details and methods

2.1. Materials

Formamidinium iodide (FAI) (≥90%, Great cell Solar (Dyesol)), Cesium iodide (CsI) (99.9%, trace metals basis, Sigma Aldrich), lead iodide (PbI_2) (99%, Sigma Aldrich), lead bromide ($PbBr_2$) (≥98%, Sigma Aldrich), tin oxide nano particle colloidal solution (SnO_2) (15% in H_2Ocolloidal dispersion, Alfa Aesar), Spiro-OMeTAD (99% HPLC, Sigma Aldrich), 4-*tert*-butylpyridine (96%, Sigma Aldrich), Bis (trifluoromethane) sulfonimide lithium salt (99.95%, Li-TFSI, trace metals basis, Sigma Aldrich), chlorobenzene (CB, anhydrous, 99.8%, Sigma Aldrich), N-N dimethylformamide (DMF, anhydrous, 99.8%, Sigma Aldrich), dimethyl sulfoxide (DMSO, anhydrous, ≥99.9%, Sigma Aldrich), Acetonitrile (anhydrous, 99.8%, Sigma Aldrich) Zinc purum powder (Sigma Aldrich), diethyl ether (DE, ≥99.5%, GC, Sigma Aldrich), isopropanol (IPA, anhydrous, 99.5%, Sigma Aldrich), hydro chloric acid (HCl, ACS reagent, 37%, Sigma Aldrich), acetone and ethanol (99%, denature, Lamberty - sarp industries, France) were used as received without any further purification.

2.2. Device fabrication

FTO-coated glass substrates were carefully etched using Zinc powder and HCl solution. Then the etched substrates were cleaned by ultrasonication in deionized water, acetone, isopropanol and ethanol for 15 mins each, before being treated by UV-ozone for 15 min. In our work, we used tin oxide as an electron transport layer (ETL) instead to titanium oxide (TiO_2). It has many advantages, such as higher electron mobility and conductivity (so, it can efficiently transfer the electrons and reduce the recombination loss), broad optical band gap value (i.e., higher transmittance it will help to absorb more photons), easier to deposit at lower temperature process, and it is stable under UV illumination. Moreover, it has a deeper conduction band; it provides excellent energy alignment with an ETL/perovskite interface for efficient electron extraction (Correa Baena et al., 2015; Jiang et al., 2018; Liu et al., 2019). The tin oxide ETL was deposited from a mother colloidal solution (1 ml) containing 10 μl of isopropanol, which was stirred for more than one hour at room temperature before the spin-coating step. A soft thermal annealing at 150 °C under air and an additional UV-ozone treatment were then applied. The ETL films were immediately transferred into a nitrogen-filled glovebox (H_2O < 0.1 ppm, O_2 < ~45 ppm) used for the perovskite film deposition. To do so, the different perovskite precursor solutions were initially prepared in the glovebox following the various recipes described below. In all cases, the suitable amounts of precursors were dissolved in a mixture of DMF (600 ml) and DMSO (78 μl): (i) For the pure $FAPbI_3$ perovskite, the precursors correspond to 172 mg of FAI and, 461 mg of PbI_2, for $FA_{0.85}Cs_{0.15}PbI_3$, (ii) then we used 146.3 mg of FAI, 39 mg of CsI, and 461 mg of PbI_2; for $FA_{0.85}Cs_{0.15}Pb(I_{0.85}Br_{0.15})_3$, and finally (iii) we used 146.3 mg of FAI, 39 mg of CsI, 392 mg of PbI_2, and 55.4 mg of $PbBr_2$.

All precursor solutions were stirred at 65 °C for about three hours. All the solutions used for device preparation were filtered using a 0.45 μm (PTFE) filter before use. The prepared perovskite solutions were spin-coated on UV-ozone treated ETL, before an anti-solvent treatment was applied by dropping 500 μl of DE onto the spinning substrate. The prepared films were transferred onto the hotplate and preheated at 100 °C for 5 mins and at 150 °C for 15 mins. For the hole transport layer (HTL), Spiro-OMeTAD, doped using Li-TFSI and 4-*tert*-butylpyridine, was deposited by spin-coating according to reported procedures (Saliba et al., 2016). After HTL deposition, the devices were immediately transferred into a high vacuum thermal evaporator where 100 nm of gold was finally deposited through a mechanical shadow mask at a pressure of 10^{-6} $mbar$ (see Fig. 1). In these conditions, the active area of the device is larger than 0.2 cm^2. Finally, we emphasize that all the particular J-V curves and device performance presented in this paper do represent the general trends observed on several devices processed in similar conditions (from 3 to 4 devices in all cases).

2.3. Characterization

An Agilent Cary 300 UV–visible spectrometer were used to measure the absorbance spectra of thin films and to calculate the absorption coefficient and the bandgap of the perovskite films. The photovoltaic performance of fabricated solar cells was extracted from measured I-V characteristics obtained using a computer-controlled Keithley 2405 source-measure unit, under simulated solar emission using a 1600 W NEWPORT solar simulator equipped with an AM1.5G filter. The irradiance was calibrated using a certified silicon detector and after spectral mismatch correction, in order to ensure a 100 $mW\ cm^{-2}$ light power density on the tested sample. The illuminated area of all devices was 0.2 cm^2 as defined by a masked aperture, and all the characterization were carried out in ambient air without encapsulation (relative moisture level of 50–60%). The parasitic series and shunt resistances (R_{series} and R_{shunt}) were extracted from simple estimation of the J-V curve slopes in open- and short-circuit conditions, assuming $R_{shunt} \gg R_{series}$. External quantum efficiency (EQE) spectra were taken from a QE-R apparatus, Enli Technology Co., Ltd in DC mode without any bias light. Similar EQE spectra were obtained using an AC modulation or a bias-light. Device cross sectional scanning electron microscope (SEM) images were recorded using a Zeiss Leo high resolution microscope.

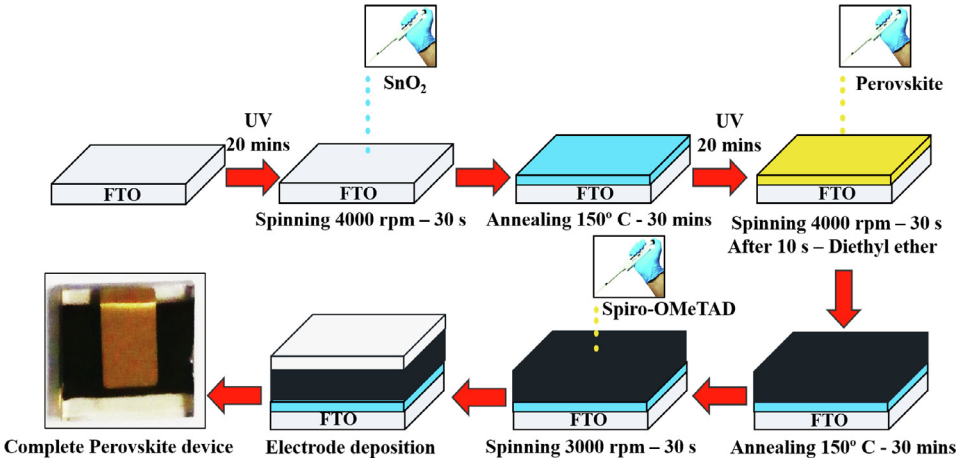

Fig. 1. Schematic representation of perovskite solar cell device fabrication.

3. Numerical simulation of ideal devices using SCAPS

One-dimensional planar n-i-p perovskite devices (FTO/SnO_2/FA perovskites/Spiro/Au) were simulated by using the Solar Cell Capacitance Simulator (SCAPS-1D) software (Burgelman et al., 2000). Three different types of FA cation-based perovskite absorber layers were used, namely pristine $FAPbI_3$, $FA_{0.85}Cs_{0.15}PbI_3$, and $FA_{0.85}Cs_{0.15}Pb(I_{0.85}Br_{0.15})_3$. The three devices are referred to D-A, D-B and D-C, respectively, for the rest of this study.

Weakly-bounded excitons are generated in the perovskite layer when the device is exposed under light. Rapid exciton dissociation then occurs before electrons and holes are rapidly collected by their respective selective contacts as depicted in Fig. 2. The simulation, which is based on a classical drift-diffusion model, is carried out at 300-K under one sun (AM1.5G, 100 $mW\ cm^{-2}$) irradiation. The optical bandgap of the active layers, as well as their thickness (around 350 nm in all cases), are obtained from experimental absorption spectra and mechanical profilometry measurements. The experimental thickness of the SnO_2 ETL (70 nm) was also used for the simulation. Other parameters, such as electron affinity, permittivity, effective density of states, charge mobility, thermal velocities, doping densities, and defect densities) were extracted from the literature (Azri et al., 2019; Chen et al., 2019; Haidari, 2019; Kuang et al., 2018; Lin et al., 2017; Tan et al., 2016), as detailed in Table 1.

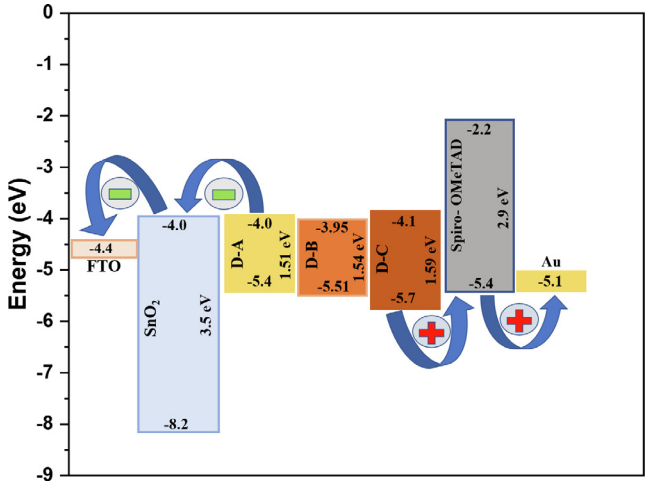

Fig. 2. Simplified flat band energy diagram of ETL, HTL and pristine $FAPbI_3$ (D-A), $FA_{0.85}Cs_{0.15}PbI_3$ (D-B) and $FA_{0.85}Cs_{0.15}Pb(I_{0.85}Br_{0.15})_3$ (D-C) perovskite active layers. FTO and Gold Fermi levels are also represented, as well as the expected charge transfer processes occurring in the final solar cells. See Table 1 for the detailed values used in this study.

4. Results and discussion

Experimental perovskite solar cells were fabricated according to the procedures reported in the above experimental section. Three active layers, namely pristine $FAPbI_3$, $FA_{0.85}Cs_{0.15}PbI_3$, and $FA_{0.85}Cs_{0.15}Pb(I_{0.85}Br_{0.15})_3$ were considered in this work in order to describe the influence of an additional cation (Cs^+) and/or halide (Br^-) on device performance.

4.1. Determination of the absorber layer bandgaps

In order to measure their thickness and optical absorption, the pristine $FAPbI_3$, $FA_{0.85}Cs_{0.15}PbI_3$, and $FA_{0.85}Cs_{0.15}Pb(I_{0.85}Br_{0.15})_3$ perovskite films were prepared on glass substrates and their optical absorption spectra were recorded using UV–visible spectroscopy (Fig. 3). The measured spectra evidence the expected absorption profile of the perovskite layer, and especially the slight blue-shift of the optical absorption edge from 835 nm down to 780 nm occurring in the presence of Br^- anion compared to the pristine or Cs-doped perovskite layer.

The optical bandgap (E_g) values of the obtained FA-perovskite films are calculated using Tauc's law in the case of a direct optical transition (Pankove and Kiewit, 1972):

$$(\alpha h\vartheta)^2 = B(h\vartheta - E_g) \quad (1)$$

where B is an independent energy constant, h is Planck's constant, α is the absorption coefficient of the perovskite film. The calculated E_g values (1.50 eV for $FAPbI_3$, 1.54 eV for $FA_{0.85}Cs_{0.15}PbI_3$, 1.59 eV for $FA_{0.85}Cs_{0.15}Pb(I_{0.85}Br_{0.15})_3$) are found in good agreement with reported trends for similar perovskite composition (Li et al., 2016; Prathapani et al., 2018). These values were used in the SCAPS simulations of devices D-A (based on pristine $FAPbI_3$), D-B (based on $FA_{0.85}Cs_{0.15}PbI_3$) and D-C (based on $FA_{0.85}Cs_{0.15}Pb(I_{0.85}Br_{0.15})_3$), respectively.

4.2. Simulation of ideal devices

In this simulation study, ideal perovskite devices are carefully optimized without considering R_{series} and R_{shunt} resistances. This step, although nonrealistic, but a good tool to evaluate the higher limit of device performance considering an optimal operation. In general, the absorber layer thickness mainly governs the level of photogenerated current, hence the overall device performance, independently of electrical losses which occurs in non-ideal devices. All the input parameters used in the simulations are given in Table 1. As already mentioned, we used the experimentally obtained thickness for ETL, HTL (165 nm), and

Table 1
Details of input parameters used for the simulation of FA-based perovskite solar cells. When data are extracted from the literature, the corresponding reference is indicated.

Parameters	FTO	ETL-(SnO_2)	D-A	D-B	D-C	HTL-(Spiro-OMeTAD)
Thickness (nm)	500*	70*	350*	350*	350*	200*
Band gap (eV)	3.5	3.5	1.51*	1.55*	1.59*	2.9
e^- affinity (eV)	4.0	4.0	4.0 (Chen et al., 2016; Tao et al., 2019)	3.95 (Prathapani et al., 2018)	4.09 (Prathapani et al., 2018)	2.2
Permittivity	9.0	9.0	6.6 (Ma et al., 2016)	6.6	6.6	3.0
Effective density of states at CB (cm^{-3})	2.2×10^{18}	2.2×10^{17}	1.2×10^{19} (Zhou and Long, 2017)	2×10^{19}	2×10^{19}	2.2×10^{18}
Effective density of states at VB (cm^{-3})	2.2×10^{18}	2.2×10^{17}	2.9×10^{18} (Gélvez-Rueda et al., 2017)	2×10^{18}	2×10^{18}	2.2×10^{18}
e^- thermal velocity (cm. s^{-1})	1×10^7	1×10^7	1×10^7	1×10^7	1×10^7	1×10^7
h^+ thermal velocity (cm. s^{-1})	1×10^7	1×10^7	1×10^7	1×10^7	1×10^7	1×10^7
Mobility of e^-(cm^2. $V^{-1}s^{-1}$)	20	20	2.7 (Gélvez-Rueda et al., 2017)	0.28 (Prathapani et al., 2018)	8.16 (Prathapani et al., 2018)	1×10^{-4}
Mobility of h^+(cm^2. $V^{-1}s^{-1}$)	10	10	1.8 (Gélvez-Rueda et al., 2017)	2	2	1×10^{-4}
Density of n-type doping (cm^{-3})	1×10^{15}	1×10^{15}	1.3×10^{16}	1.3×10^{16}	1.3×10^{16}	0
Density of p-type doping (cm^{-3})	0	0	1.3×10^{16}	1.3×10^{16}	1.3×10^{16}	1.3×10^{18}
Density of defects (cm^{-3})	10^{18}	10^{18}	4×10^{13}	4×10^{13}	4×10^{13}	10^{15}

*Indicates this current work.

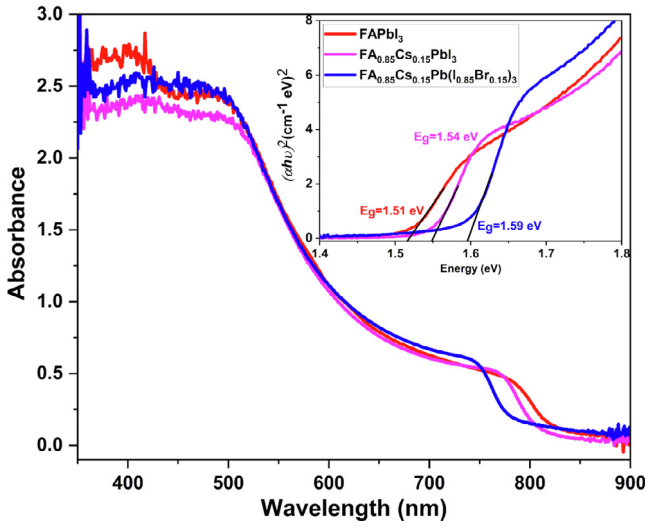

Fig. 3. UV–visible absorbance spectra of pristine $FAPbI_3$, $FA_{0.85}Cs_{0.15}PbI_3$, and $FA_{0.85}Cs_{0.15}Pb(I_{0.85}Br_{0.15})_3$ perovskite films. The inset shows the corresponding Tauc's plot used for bandgap calculations.

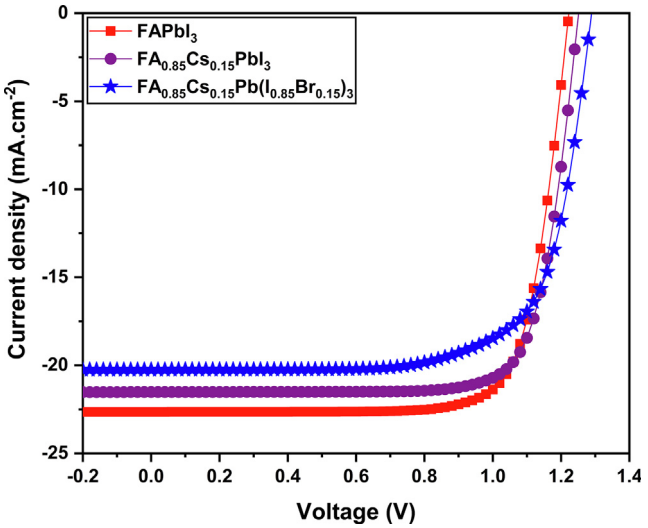

Fig. 4. Simulated J-V characteristics of ideal D-A, D-B and D-C perovskite devices, respectively.

perovskite active layers, as well as optical bandgap values of the three absorber layers. The simulated photovoltaic parameters do not change much as a function of the HTL thickness values (see SI, Table S1), therefore, all the simulations we used 200 nm. Additionally, all other parameters such as electron affinity, dielectric permittivity, effective densities of states at conduction and valence bands, as well as electron e^- and hole h^+ mobility values were taken from previously published results (Chen et al., 2016; Gélvez-Rueda et al., 2017; Ma et al., 2016; Prathapani et al., 2018; Tao et al., 2019; Zhou and Long, 2017). Some of these parameters were optimized in order to achieve reproducible and consistent results.

Fig. 4 displays the optimized current-voltage characteristics (J-V) of the three ideal devices from which the main photovoltaic parameters are extracted: short-circuit density (J_{sc}), fill factor (FF), open circuit voltage (V_{oc}) and power conversion efficiency (PCE). These values are summarized and presented in Table 2.

Considering similar active layer thicknesses, this first level of simulation shows that pristine $FAPbI_3$ device (D-A) demonstrates the highest PCE, compared to the others. This behavior is the result of trend

Table 2
Summarized photovoltaic parameters of ideal devices D-A, D-B and D-C, respectively.

Device	J_{SC} (mA/cm^{-2})	FF (%)	V_{oc} (V)	PCE (%)
D-A	22.6	77	1.2	21.4
D-B	21.5	78	1.2	21.0
D-C	20.2	72	1.3	18.7

between the variation of optical bandgaps and charge mobilities (especially for electrons). As a consequence, a significant decrease is observed in J_{sc} value from 22.6 mA/cm^{-2} down to 20.2 mA/cm^{-2} for D-A and, D-C devices, respectively. This trend is confirmed by the simulated current density - voltage slope (shown in Fig. 4). Consequently, all the simulated devices are displaying good efficiencies in the absence of parasitic electrical losses, which is indicating suitable optoelectronic properties of the active layers (suitable charge carrier mobilities), as well as suitable energy band alignment with the SnO_2 (ETL) and Spiro-OMeTAD (HTL) interfacial layers (Fig. 2).

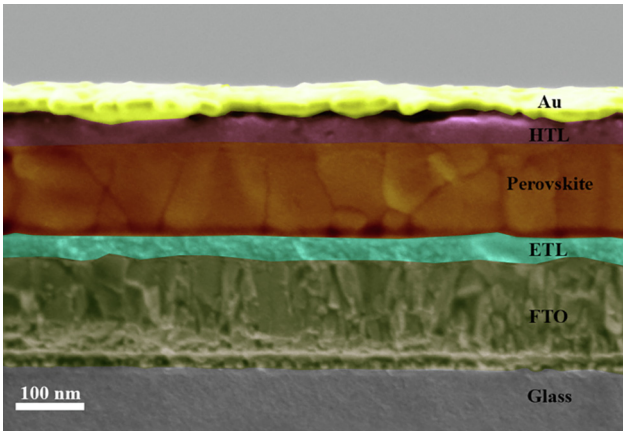

Fig. 5. Cross sectional SEM image of FTO/$SnO_2/FA_{0.85}Cs_{0.15}Pb(I_{0.85}Br_{0.15})_3$/Spiro/Au device.

4.3. Experimental devices

From the experimental point of view, we successfully fabricated the D-A, D-B and D-C devices using a simple one-step solution process with anti-solvent strategy (see experimental details). Note that all devices were processed and characterized in ambient conditions, expect the perovskite active layer deposition, which is processed under a nitrogen-filled glovebox. The typical morphology of a device is illustrated in Fig. 5 which shows the SEM cross-section of device D-C. The image demonstrates a very good homogeneity of the sandwich structure, with a quite compact perovskite layer. Such observation is particularly consistent with the performed SCAPS simulation using a planar structure.

The experimental J-V curves were recorded under simulated solar irradiation calibrated to achieve one sun illumination conditions (AM1.5G). They are displayed in Fig. 6 below. The corresponding photovoltaic parameters are presented in the Table 3. Again, both forward and backward scans are available as supporting information (Fig. S1 and Table S2).

Unsurprisingly, the experimental performance is found to be much less than the simulated case, especially for device D-A, which corresponds to the pure FA-based lead iodide active layer (PCE of 4.3% only). Independently to the fact that ideal devices were simulated and compared to experimental non-ideal devices, the main origin that

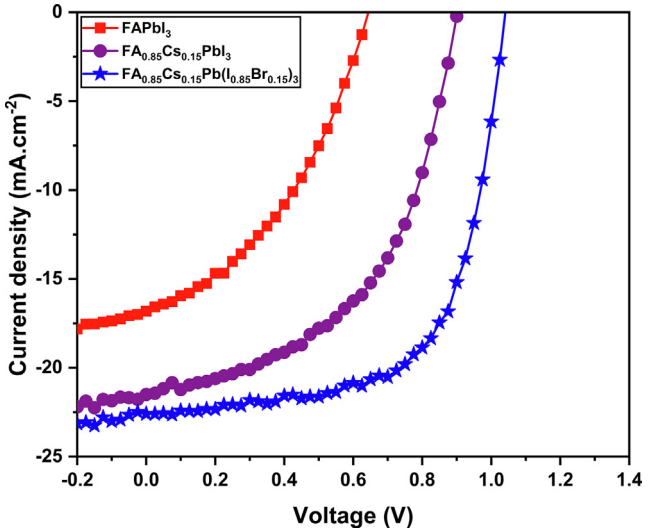

Fig. 6. Experimental J-V characteristics of D-A, D-B and D-C perovskite devices, respectively.

Table 3
Recorded photovoltaic parameters of experimental devices D-A, D-B and D-C, respectively.

Device	J_{SC} (mA/cm^{-2})	FF (%)	V_{oc} (V)	PCE (%)
D-A	16.6	40.6	0.6	4.3
D-B	21.4	51.6	0.9	9.9
D-C	22.6	64.4	1.0	15.1

explains this observation is associated with the instability of the $FAPbI_3$ $\alpha - phase$. In our processing conditions, we indeed observed a fast color change from black to yellow for the active layer of device D-A, as illustrated in Fig. 7, while devices D-B and D-C remains dark brown in the same conditions.

There are several reasons reported (i.e., moisture, humidity, presence of water/solvents in formamidinium) to explain this behavior, especially considering the relatively high level of moisture of our laboratory (> 50%). For example, a high humidity level is usually associated with larger voids in the film, which gradually degrade the active layer properties, leading to low PCE (Wozny et al., 2015; Yun et al., 2018). Therefore, we only show preliminary stability assessments which however are quite consistent with reported trends, as explained previously. This phenomenon is also usually associated with a large hysteresis effect, which can be seen here for device D-A (refer SI).

Device D-B which incorporates Cesium demonstrates a much improved PCE of ~10% in forward scan. Notably, the hysteresis effect is reduced compared to D-A device, which can be due to their excellent resistance against the phase segregation (i.e., black to yellow phase conversion) and the higher thermal healing behavior (i.e., at high temperature, lower weight loss occurred in $FA_{0.85}Cs_{0.15}PbI_3$ than $FAPbI_3$ (Huang et al., 2017)) (see SI, Fig. S1). The incorporation of Cs^+ cations into $FAPbI_3$ is known to reduce the decomposition of the perovskite structure, leading to a reduced formation of PbI_2. Consequently, it stabilizes the black phase (as observed in Fig. 7) which is another prominent reason for the PCE improvement (Li et al., 2016). Extraction of the experimental parasitic resistances gives higher R_{shunt} and lower R_{series} values, which of course comes with this PCE enhancement. We also emphasize, as reported in the literature, that the stability of $FA - Cs$ devices is mainly attributed to the stronger interactions between FA cations and I halogens because of their cubo-octahedral volume reduction than the undoped device (Lee et al., 2015).

Finally, doping the $FA - Cs$ perovskite film with bromide leads to the wider band gap layer, but also to the device (D-C) displaying the highest (champion) PCE of 15.1%. We noticed that all the photovoltaic parameters (PCE, J_{sc}, FF, V_{oc}) are largely improved for device D-C compared to devices D-A and D-B. This observation is in line with reported studies which have shown that the presence of Bromide further enhances the crystallinity and the stability of the 3D formamidinium lead iodide cubic phase, this behavior being associated with the accumulation of strain due to the halide incorporation, and their photocarrier recombination phenomenon (Rehman et al., 2017). The obtained results are thus showing good agreement with previously published reports (Correa Baena et al., 2015), which emphasize that the SnO_2 ETL clearly shows an excellent band alignment with mixed cation/halide perovskite material than pristine one, especially in the planar n-i-p configuration.

The spectral response of different perovskite solar devices is represented by EQE as a function of wavelength of incident light. Both experimental and simulated EQE spectra were shown in Fig. 8, corresponding to D-A, D-B and D-C devices, respectively. Note that the simulated EQE curves are generated from the ideal devices, which means optical reflection of each layers, interfaces and both resistances (R_{shunt} and R_{series}) are not considered. The following equation representing the traditional SCAPS optical absorption model with $sqrt(h\nu - E_g)$ submodel, which is used for all the EQE spectra simulation, by means of the

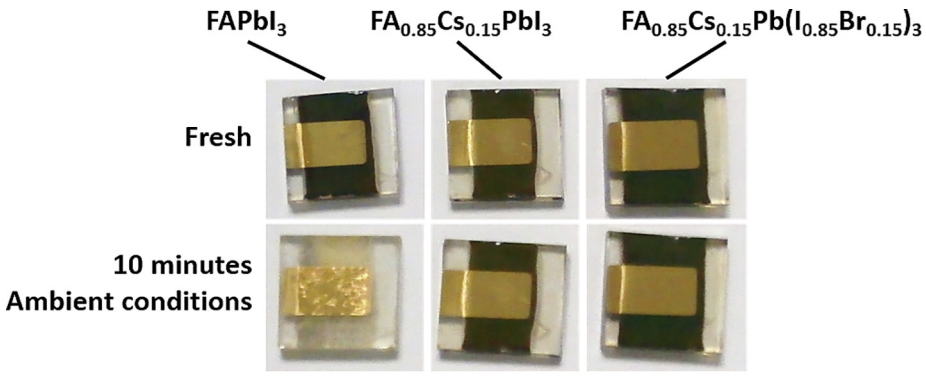

Fig. 7. Photographs of fresh (top) and exposed to air for 10 min (bottom) D-A, D-B and D-C devices.

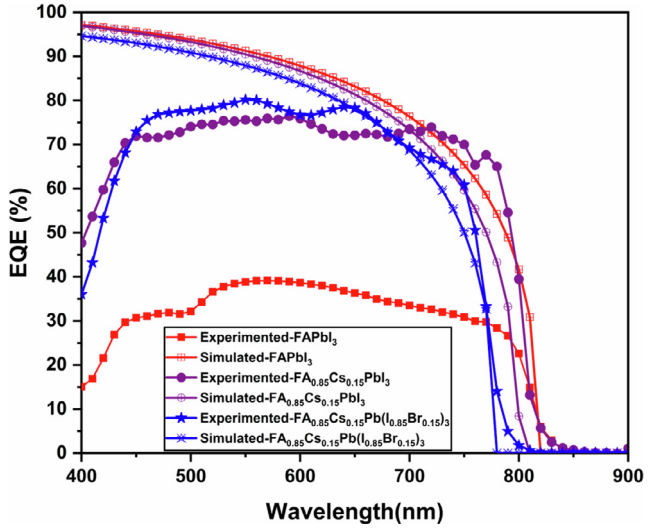

Fig. 8. External quantum efficiency spectra of experimental and simulated (D-A, D-B and D-C) perovskite solar cells.

bandgap, always depend on the provided E_g value as one of the electronic properties of the layer (Burgelman et al., 2000).

$$\alpha(\lambda) = \left(A + \frac{B}{h\nu}\right)\sqrt{h\nu - E_g} \tag{2}$$

Whereα is the optical absorption constant, E_g is the actual band of the layer, A and$B$ are the absorption parameters which is normally set to $1.00E+5$ and $1.00E-12$, respectively.

Due to the narrow and wider absorber layer bandgap of device D-A to D-C, optical absorption edge shifts from 830 nm to 780 nm and the obtained EQE curves cover the complete visible spectrum from 400 nm to 700 nm shown in Fig. 8. The experimental EQE of device D-A is showing lower efficiency due to the fact that the device shows a strong degradation and phase instability, as mentioned previously, meanwhile, D-B & D-C significantly holds more than 70% quantum efficiency. In practical, experimental devices suffer from the different kind of losses, such as recombination loss and absorption loss. As we mentioned before, the simulated device spectra were calculated using SCAPS, taking into account the experimental bandgaps of the active layer, without considering the optical effects (such as without total reflection) and the recombination losses. Moreover, it looks more similar to the ideal solar device behavior (such as rectangular shape), this is probably due to the absorption law that is used by SCAPS to model the absorption profile of the semiconductors. The resistance losses (R_{shunt} and R_{series}) and ionic immigration could be the main reasons for the disagreement between simulated EQE representation to the experimental one (Haidari, 2019).

We see a strong correlation between the experimental and simulated EQE spectra, as they exhibit similar trends regarding the active layer spectral sensitivity range as a function of perovskite composition. The Br-doped layer is displaying a reduced sensitivity window (device D-C), in accordance with its larger bandgap value compared to the $FA-Cs$ layer (device D-B). Moreover, it is possible to relate the EQE spectra to the measured short-circuit current densities, as described by the equation (Rau, 2007):

$$J_{SC} = q\int F(\lambda).\, EQE(\lambda)d(\lambda) \tag{3}$$

where, $F(\lambda)$ is the photon flux and q is the elementary charge.

The obtained experimental EQE J_{sc} values 9.10 mA/cm^{-2} (D-A), 19.38 mA/cm^{-2} (D-B) and 21.63 mA/cm^{-2} (D-C) provides an excellent agreement with measured J_{sc}, shown in Table 3.

From this first approach, the obtained experimental and simulated ideal devices show different behaviors. First, the simulated D-A device (pure $FAPbI_3$) exhibits a much higher PCE than the experimental one. This can be attributed to the spontaneous and rapid phase transition from the optically active $\alpha-phase$ (black) to the inactive $\delta-phase$ (yellow). This transition is found to be particularly fast in our ambient conditions, due to the presence of a high level of moisture and oxygen. The SCAPS simulation does not account for this effect, resulting in a very efficient devices. Then, we observed that the simulated D-B and D-C devices are better describing the experimental trends in terms of photocurrent, due to the consistent influence of the optical bandgap of the layers. However, the experimental devices are obviously largely limited by parasitic resistances. Indeed, several phenomena, such as defect states (especially surface and interface states) or some local inhomogeneity in the sandwich structure, lead to charge recombination or current leakages, which introduce series (R_{series}) and shunt (R_{shunt}) parasitic resistances. Therefore, we now analyze the effect of these resistances in order to point out the exact influence of cesium and bromide in device operation.

4.4. Effect of R_{series} and R_{shunt}

Both R_{shunt} and R_{series} resistances have a crucial impact on device performance, as they govern the shape and slopes of the J-V characteristics. Basically, R_{series} finds its origin in the electrical resistance associated with contacts (FTO and gold), but also with the electrical dissipation occurring in the ETL, HTL, and active layer. R_{shunt}, which is the manifestation of several alternative charge recombination paths, is also highly influenced by the device design (edge effects). Consequently, a low R_{shunt} results in a photovoltage loss and can also affect the collected photocurrent. In parallel, R_{series} mainly affects the FF and short-circuit current values. It is well known that a low R_{series} and a high R_{shunt} should be achieved in order to demonstrate highly efficient devices. In a first and quite general approach, the following equation is used to understand the consequences of R_{shunt} and R_{series} on the ideal single-diode device performance (Li et al., 2017):

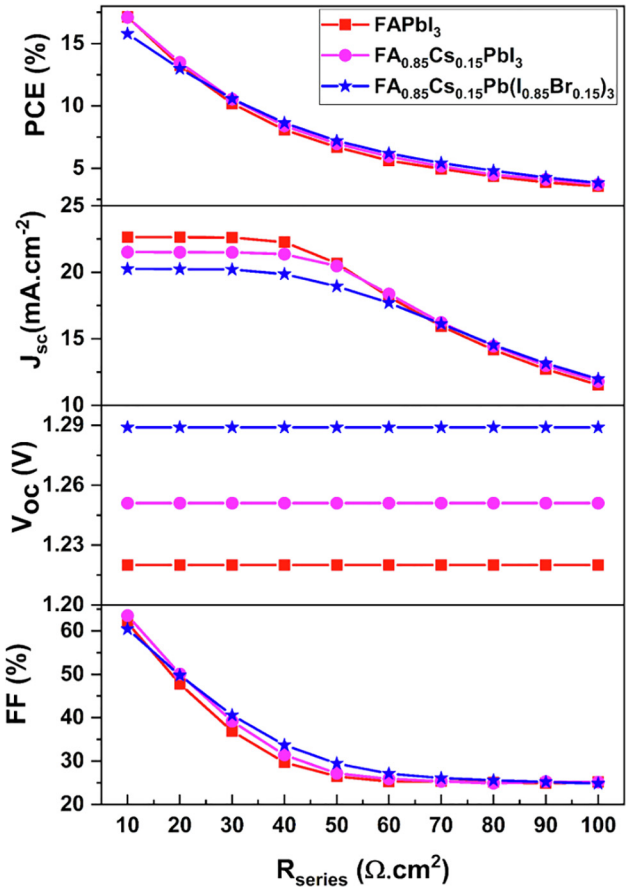

Fig. 9. Effect of R_{series} in the performance of simulated D-A, D-B and D-C devices. R_{shunt} is assumed as infinite in this case.

$$I = I_L - I_0\left[e^{\left(\frac{q(M)}{AkBT}\right)} - 1\right] - \left(\frac{M}{R_{Shunt}}\right) \quad (3)$$

where, $M = V + S$, $S = I * R_{series}$, I_L is the light-induced current, I_0 is the reverse saturation current of the diode, A is ideality factor, k_B is Boltzmann constant, T is temperature and q is charge of the electron.

To understand the effect of R_{series} and R_{shunt} on ideal device characteristics, we introduced them in the SCAPS model and varied their values between 10–100 Ω. cm^2 and 500–5000 Ω. cm^2, respectively. The corresponding evolutions of the main photovoltaic parameters are shown in Fig. 9 and Fig. 10.

Our results clearly illustrate that an increase in R_{series} strongly reduces the FF from 60% to 25% for all types of devices. Moreover, for a R_{series} over 30 Ω. cm^2 J_{SC} is rapidly reduced for all three devices, down to 12 mA/cm^{-2}.The overall power conversion efficiency is therefore rapidly decreasing from 18% to only 4% (see Fig. 9). Normally, V_{OC} is not affected by the R_{series}, the obtained V_{OC} behavior of D-A, D-B, and D-C devices are demonstrated in Fig. 9. In parallel, increasing R_{shunt} leads to a rapid increase in FF and PCE values (Fig. 10), While V_{OC} and J_{SC} are only slightly affected by R_{shunt}, the better fill factor mainly explains the improvement in device performance here.

Following these general trends in device behavior which are obviously consistent with the reported literature on photovoltaic device performance and simulation, we finally tried to feed our SCAPS simulations using the experimental values of parasitic resistances (R_{series} and R_{shunt}) extracted from the measured J-V characteristics shown in Fig. 6. The simulated J-V characteristics obtained for devices D-A, D-B, and D-C in these conditions are plot in Fig. 11 below, while Table 4. summarizes the photovoltaic parameters obtained on experimental and non-ideal simulated devices. Considerable changes are now occurring

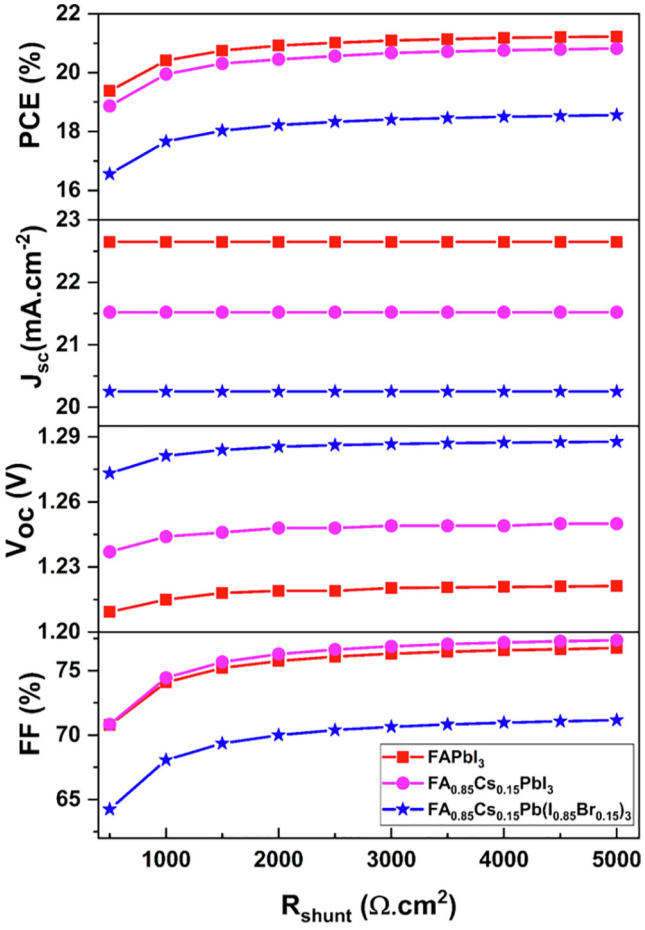

Fig. 10. Effect of R_{shunt} in the D-A, D-B and D-C performance.

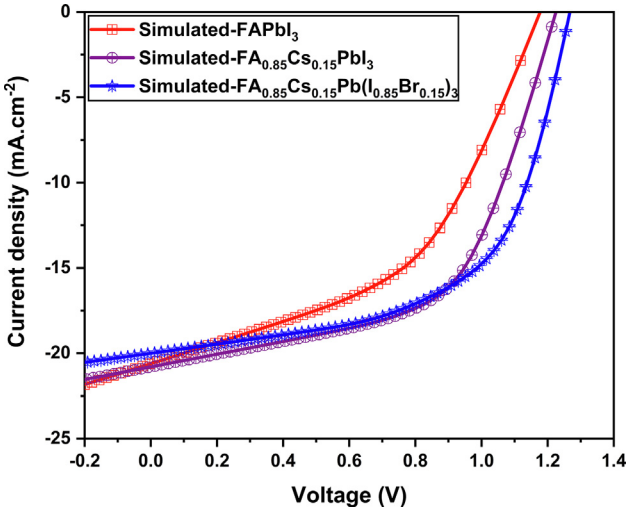

Fig. 11. Simulated J-V characteristic results of D-A, D-B and D-C.

for the performance of the simulated devices. All photovoltaic parameters are impacted by the parasitic resistances, which is clearly expected as discussed previously.

After feeding R_{series} and R_{shunt} values into the simulated D-A, D-B and D-C devices, we noticed the performances were decreasing compared to ideal devices, as shown in Table 4. Interestingly, this simple approach shows that the slopes at open-circuit and short-circuit of the simulated J-V characteristics are comparable to experimental data (as pointed out in Fig. S1, in SI). The high V_{oc}, FF, and J_{SC} value of the mixed cation

Table 4
Comparison of experimental FW scan device performances of D-A, D-B and D-C with the simulated devices (after feeding R_{series} and R_{shunt}).

Device	Data	Scan	J_{SC} mA/cm^{-2}	FF (%)	V_{oc} (V)	PCE (%)	R_{series} (Ω)	R_{shunt} (Ω)
D-A	Ex	FW	16.6	40.6	0.6	4.3	73	744
	Sim		20.6	47.4	1.1	11.5		
D-B	Ex	FW	21.4	51.6	0.9	9.9	45	1312
	Sim		20.8	56.9	1.2	14.5		
D-C	Ex	FW	22.6	64.4	1.0	15.1	22	1854
	Sim		20.0	58.2	1.2	14.7		

(Cs^+) mixed halide (Br^-) device in terms of improved electronic properties: electron mobility which is highly improved (so a lower R_{series}). Probably also there is less defect states and interface states, which are responsible for higher R_{shunt}. V_{oc} is also improved due to the larger bandgap (as the conduction band is less deep), so the theoretical V_{oc} should be larger.

Cs^+ and Br^- incorporated D-B and D-C devices showing a highly improved FF value compared to device D-A due to their improved charge transfer capacity. Especially, absorber layer of device D-C exhibiting the n-type semi-conducting behavior by means of an electron being the majority carrier (as mentioned before, high charge carrier mobility) (Prathapani et al., 2018). In addition, both long charge carrier diffusion length and the slow recombination kinetics also strongly modifies the photovoltaic performance (McMeekin et al., 2016; Rehman et al., 2017), those are the main reasons for their enhanced device performance than other two, shown in Table 1 and Table 4.

5. Conclusion

In this work, experimental and numerically simulated performance of planar FA-based perovskite solar cells is investigated and presented. First, our experimental devices clearly illustrate that the incorporation of both Cs^+ and Br^- ions in the $FAPbI_3$ perovskite structure (device D-C) is leading to the highest photovoltaic response among the tested devices, with a power conversion efficiency above 15%. This performance is a consequence of an improved stability in ambient conditions. SCAPS simulations of ideal devices with ideal parasitic resistances confirmed that the pure FA-based perovskite is the most interesting active layer to achieve high photocurrents, due to its lower optical bandgap. However, its instability in open air justifies the use of stabilizing ions such as Cesium or Bromide. Moreover, real devices can be fully understood only by accounting for reasonable series and shunt resistances, which allow the consideration of recombination losses or leakages. Using this strategy, using SCAPS, we were able to estimate the influence of Cesium and Bromide on the FA-based perovskite active layer performance. The combination of both elements is responsible for an improvement of device operation through improved charge transport, reduced recombination, and better stability in ambient conditions. A good correlation between experimental and simulated devices can lead to a better understanding in the charge generation mechanism and active layer performance.

Declaration of Competing Interest

The authors declared that there is no conflict of interest.

Acknowledgements

The author S. Karthick gratefully to CONACYT for the doctoral fellowship granted. This work is partially supported by the project CONACyT-SENER 263043. Also this work is benefited from the French government support managed by the National Research Agency under the Investments for the future program with the reference ANR-10-LABX-0074-01 Sigma-LIM. J.B. is thankful to Nicolas Parou and the PLATINOM technology platform (common facility of the University of Limoges) which hosted all steps regarding device fabrication and characterization. The CARMALIM common facility (University of Limoges, Limoges) is also acknowledged, as well as E. Hyvernaud for SEM measurements.

Appendix A. Supplementary material

Supplementary data to this article can be found online at https://doi.org/10.1016/j.solener.2020.05.041.

References

Abdelaziz, S., Zekry, A., Shaker, A., Abouelatta, M., 2020. Investigating the performance of formamidinium tin-based perovskite solar cell by SCAPS device simulation. Opt. Mater. (Amst). https://doi.org/10.1016/j.optmat.2020.109738.

Azri, F., Meftah, Afak, Sengouga, N., Meftah, Amjad, 2019. Electron and hole transport layers optimization by numerical simulation of a perovskite solar cell. Sol. Energy. https://doi.org/10.1016/j.solener.2019.02.017.

Burgelman, M., Nollet, P., Degrave, S., 2000. Modelling polycrystalline semiconductor solar cells. Thin Solid Films. https://doi.org/10.1016/S0040-6090(99)00825-1.

Bush, K.A., Palmstrom, A.F., Yu, Z.J., Boccard, M., Cheacharoen, R., Mailoa, J.P., McMeekin, D.P., Hoye, R.L.Z., Bailie, C.D., Leijtens, T., Peters, I.M., Minichetti, M.C., Rolston, N., Prasanna, R., Sofia, S., Harwood, D., Ma, W., Moghadam, F., Snaith, H.J., Buonassisi, T., Holman, Z.C., Bent, S.F., McGehee, M.D., 2017. 23.6%-efficient monolithic perovskite/silicon tandem solar cells with improved stability. Nat. Energy. https://doi.org/10.1038/nenergy.2017.9.

Chen, Y., Hu, Y., Meng, Q., Yan, H., Shuai, W., Zhang, Z., 2019. Natively textured surface of Ga-doped ZnO films electron transporting layer for perovskite solar cells: further performance analysis from device simulation. J. Mater. Sci.: Mater. Electron. https://doi.org/10.1007/s10854-019-00766-7.

Chen, L.C., Tseng, Z.L., Huang, J.K., 2016. A study of inverted-type perovskite solar cells with various composition ratios of (FAPBI3)1–x(MAPbBr 3)x. Nanomaterials. https://doi.org/10.3390/nano6100183.

Correa Baena, J.P., Steier, L., Tress, W., Saliba, M., Neutzner, S., Matsui, T., Giordano, F., Jacobsson, T.J., Srimath Kandada, A.R., Zakeeruddin, S.M., Petrozza, A., Abate, A., Nazeeruddin, M.K., Grätzel, M., Hagfeldt, A., 2015. Highly efficient planar perovskite solar cells through band alignment engineering. Energy Environ. Sci. https://doi.org/10.1039/c5ee02608c.

Eperon, G.E., Stranks, S.D., Menelaou, C., Johnston, M.B., Herz, L.M., Snaith, H.J., 2014. Formamidinium lead trihalide: A broadly tunable perovskite for efficient planar heterojunction solar cells. Energy Environ. Sci. https://doi.org/10.1039/c3ee43822h.

Galkowski, K., Mitioglu, A., Miyata, A., Plochocka, P., Portugall, O., Eperon, G.E., Wang, J.T.W., Stergiopoulos, T., Stranks, S.D., Snaith, H.J., Nicholas, R.J., 2016. Determination of the exciton binding energy and effective masses for methylammonium and formamidinium lead tri-halide perovskite semiconductors. Energy Environ. Sci. https://doi.org/10.1039/c5ee03435c.

Gélvez-Rueda, M.C., Renaud, N., Grozema, F.C., 2017. Temperature dependent charge carrier dynamics in formamidinium lead iodide perovskite. J. Phys. Chem. C. https://doi.org/10.1021/acs.jpcc.7b09303.

Groeneveld, B.G.H.M., Adjokatse, S., Nazarenko, O., Fang, H.H., Blake, G.R., Portale, G., Duim, H., ten Brink, G.H., Kovalenko, M.V., Loi, M.A., 2020. Stable cesium formamidinium lead halide perovskites: a comparison of photophysics and phase purity in thin films and single crystals. Energy Technol. https://doi.org/10.1002/ente.201901041.

Haidari, G., 2019. Comparative 1D optoelectrical simulation of the perovskite solar cell. AIP Adv. https://doi.org/10.1063/1.5110495.

Han, Q., Bae, S.H., Sun, P., Hsieh, Y.T., Yang, Y., Rim, Y.S., Zhao, H., Chen, Q., Shi, W., Li, G., Yeng, Y., 2016. Single crystal formamidinium lead iodide (FAPbI3): insight into the structural, optical, and electrical properties. Adv. Mater. https://doi.org/10.1002/adma.201505002.

Hu, Z., Xiang, H., Schoenauer Sebag, M., Billot, L., Aigouy, L., Chen, Z., 2018. Compact layer free mixed-cation lead mixed-halide perovskite solar cells. Chem. Commun. https://doi.org/10.1039/c7cc06183h.

Huang, J., Xu, P., Liu, J., You, X.Z., 2017. Sequential introduction of cations deriving large-grain CsxFA1 − xPbI3 thin film for planar hybrid solar cells: insight into phase-segregation and thermal-healing behavior. Small. https://doi.org/10.1002/smll.

201603225.
Jiang, Q., Zhang, X., You, J., 2018. SnO2: a wonderful electron transport layer for perovskite solar cells. Small. https://doi.org/10.1002/smll.201801154.
Kuang, Y., Zardetto, V., Van Gils, R., Karwal, S., Koushik, D., Verheijen, M.A., Black, L.E., Weijtens, C., Veenstra, S., Andriessen, R., Kessels, W.M.M., Creatore, M., 2018. Low-temperature plasma-assisted atomic-layer-deposited SnO2 as an electron transport layer in planar perovskite solar cells. ACS Appl. Mater. Interfaces. https://doi.org/10.1021/acsami.8b09515.
Lee, J.W., Kim, D.H., Kim, H.S., Seo, S.W., Cho, S.M., Park, N.G., 2015. Formamidinium and cesium hybridization for photo- and moisture-stable perovskite solar cell. Adv. Energy Mater. https://doi.org/10.1002/aenm.201501310.
Li, Y., Ding, B., Chu, Q.Q., Yang, G.J., Wang, M., Li, C.X., Li, C.J., 2017. Ultra-high open-circuit voltage of perovskite solar cells induced by nucleation thermodynamics on rough substrates. Sci. Rep. https://doi.org/10.1038/srep46141.
Li, Z., Yang, M., Park, J.S., Wei, S.H., Berry, J.J., Zhu, K., 2016. Stabilizing perovskite structures by tuning tolerance factor: formation of formamidinium and cesium lead iodide solid-state alloys. Chem. Mater. https://doi.org/10.1021/acs.chemmater.5b04107.
Lin, L., Jiang, L., Qiu, Y., Yu, Y., 2017. Modeling and analysis of HTM-free perovskite solar cells based on ZnO electron transport layer. Superlattices Microstruct. https://doi.org/10.1016/j.spmi.2017.02.028.
Liu, D., Wang, Y., Xu, H., Zheng, H., Zhang, T., Zhang, P., Wang, F., Wu, J., Wang, Z., Chen, Z., Li, S., 2019. SnO2-based perovskite solar cells: configuration design and performance improvement. Sol. RRL. https://doi.org/10.1002/solr.201800292.
Ma, F., Li, J., Li, W., Lin, N., Wang, L., Qiao, J., 2016. Stable α/δ phase junction of formamidinium lead iodide perovskites for enhanced near-infrared emission. Chem. Sci. https://doi.org/10.1039/c6sc03542f.
McMeekin, D.P., Sadoughi, G., Rehman, W., Eperon, G.E., Saliba, M., Hörantner, M.T., Haghighirad, A., Sakai, N., Korte, L., Rech, B., Johnston, M.B., Herz, L.M., Snaith, H.J., 2016. A mixed-cation lead mixed-halide perovskite absorber for tandem solar cells. Science (80-). https://doi.org/10.1126/science.aad5845.
Nazarenko, O., Yakunin, S., Morad, V., Cherniukh, I., Kovalenko, M.V., 2017. Single crystals of caesium formamidinium lead halide perovskites: Solution growth and gamma dosimetry. NPG Asia Mater. https://doi.org/10.1038/am.2017.45.
NREL, 2019. Best Research-Cell Efficiency Chart | Photovoltaic Research | NREL. Best Res. Effic. Chart | Photovolt. Res. | NREL.
Pang, S., Hu, H., Zhang, J., Lv, S., Yu, Y., Wei, F., Qin, T., Xu, H., Liu, Z., Cui, G., 2014. NH2CH=NH2PbI3: An alternative organolead iodide perovskite sensitizer for mesoscopic solar cells. Chem. Mater. https://doi.org/10.1021/cm404006p.
Pankove, J.I., Kiewit, D.A., 1972. Optical processes in semiconductors. J. Electrochem. Soc. https://doi.org/10.1149/1.2404256.
Prathapani, S., Bhargava, P., Mallick, S., 2018. Electronic band structure and carrier concentration of formamidinium-cesium mixed cation lead mixed halide hybrid perovskites. Appl. Phys. Lett. https://doi.org/10.1063/1.5016829.
Prochowicz, D., Runjhun, R., Tavakoli, M.M., Yadav, P., Saski, M., Alanazi, A.Q., Kubicki, D.J., Kaszkur, Z., Zakeeruddin, S.M., Lewiński, J., Grätzel, M., 2019. Engineering of perovskite materials based on formamidinium and cesium hybridization for high-efficiency solar cells. Chem. Mater. https://doi.org/10.1021/acs.chemmater.8b04871.
Rau, U., 2007. Reciprocity relation between photovoltaic quantum efficiency and electroluminescent emission of solar cells. Phys. Rev. B - Condens. Matter Mater. Phys. https://doi.org/10.1103/PhysRevB.76.085303.
Rehman, W., McMeekin, D.P., Patel, J.B., Milot, R.L., Johnston, M.B., Snaith, H.J., Herz, L.M., 2017. Photovoltaic mixed-cation lead mixed-halide perovskites: Links between crystallinity, photo-stability and electronic properties. Energy Environ. Sci. https://doi.org/10.1039/c6ee03014a.
Saliba, M., Matsui, T., Seo, J.Y., Domanski, K., Correa-Baena, J.P., Nazeeruddin, M.K., Zakeeruddin, S.M., Tress, W., Abate, A., Hagfeldt, A., Grätzel, M., 2016. Cesium-containing triple cation perovskite solar cells: Improved stability, reproducibility and high efficiency. Energy Environ. Sci. https://doi.org/10.1039/c5ee03874j.
Shallcross, R.C., Zheng, Y., Saavedra, S.S., Armstrong, N.R., 2017. Determining band-edge energies and morphology-dependent stability of formamidinium lead perovskite films using spectroelectrochemistry and photoelectron spectroscopy. J. Am. Chem. Soc. https://doi.org/10.1021/jacs.7b00516.
Sutter-Fella, C.M., Ngo, Q.P., Cefarin, N., Gardner, K.L., Tamura, N., Stan, C.V., Drisdell, W.S., Javey, A., Toma, F.M., Sharp, I.D., 2018. Cation-dependent light-induced halide demixing in hybrid organic-inorganic perovskites. Nano Lett. https://doi.org/10.1021/acs.nanolett.8b00541.
Tan, K., Lin, P., Wang, G., Liu, Y., Xu, Z., Lin, Y., 2016. Controllable design of solid-state perovskite solar cells by SCAPS device simulation. Solid. State. Electron. https://doi.org/10.1016/j.sse.2016.09.012.
Tao, S., Schmidt, I., Brocks, G., Jiang, J., Tranca, I., Meerholz, K., Olthof, S., 2019. Absolute energy level positions in tin- and lead-based halide perovskites. Nat. Commun. https://doi.org/10.1038/s41467-019-10468-7.
Wang, Z., McMeekin, D.P., Sakai, N., van Reenen, S., Wojciechowski, K., Patel, J.B., Johnston, M.B., Snaith, H.J., 2017. Efficient and air-stable mixed-cation lead mixed-halide perovskite solar cells with n-doped organic electron extraction layers. Adv. Mater. https://doi.org/10.1002/adma.201604186.
Wozny, S., Yang, M., Nardes, A.M., Mercado, C.C., Ferrere, S., Reese, M.O., Zhou, W., Zhu, K., 2015. Controlled humidity study on the formation of higher efficiency formamidinium lead triiodide-based solar cells. Chem. Mater. https://doi.org/10.1021/acs.chemmater.5b01691.
Yang, M., Kim, D.H., Yu, Y., Li, Z., Reid, O.G., Song, Z., Zhao, D., Wang, C., Li, L., Meng, Y., Guo, T., Yan, Y., Zhu, K., 2018. Effect of non-stoichiometric solution chemistry on improving the performance of wide-bandgap perovskite solar cells. Mater. Today Energy. https://doi.org/10.1016/j.mtener.2017.10.001.
Yi, C., Luo, J., Meloni, S., Boziki, A., Ashari-Astani, N., Grätzel, C., Zakeeruddin, S.M., Röthlisberger, U., Grätzel, M., 2016. Entropic stabilization of mixed A-cation ABX3 metal halide perovskites for high performance perovskite solar cells. Energy Environ. Sci. https://doi.org/10.1039/c5ee03255e.
Yu, Y., Wang, C., Grice, C.R., Shrestha, N., Chen, J., Zhao, D., Liao, W., Cimaroli, A.J., Roland, P.J., Ellingson, R.J., Yan, Y., 2016. Improving the performance of formamidinium and cesium lead triiodide perovskite solar cells using lead thiocyanate additives. ChemSusChem. https://doi.org/10.1002/cssc.201601027.
Yun, J.S., Kim, J., Young, T., Patterson, R.J., Kim, D., Seidel, J., Lim, S., Green, M.A., Huang, S., Ho-Baillie, A., 2018. Humidity-induced degradation via grain boundaries of HC(NH2)2PbI3 planar perovskite solar cells. Adv. Funct. Mater. https://doi.org/10.1002/adfm.201705363.
Zhou, Y., Long, G., 2017. Low density of conduction and valence band states contribute to the high open-circuit voltage in perovskite solar cells. J. Phys. Chem. C. https://doi.org/10.1021/acs.jpcc.6b10914.
Zhumekenov, A.A., Saidaminov, M.I., Haque, M.A., Alarousu, E., Sarmah, S.P., Murali, B., Dursun, I., Miao, X.H., Abdelhady, A.L., Wu, T., Mohammed, O.F., Bakr, O.M., 2016. Formamidinium lead halide perovskite crystals with unprecedented long carrier dynamics and diffusion length. ACS Energy Lett. https://doi.org/10.1021/acsenergylett.6b00002.